# $MnO_2$ Superstructure Cathode with Boosted Zinc Ion Intercalation for Aqueous Zinc Ion Batteries

Aina Zhang[1]#, Xu Zhang[1]#, Hainan Zhao[1,2], Helmut Ehrenberg[2], Gang Chen[1], Ismael Saadoune[3], Qiang Fu[2]*, Yingjin Wei[1], and Yizhan Wang[1]*
1. Key Laboratory of Physics and Technology for Advanced Batteries (Ministry of Education), College of Physics, Jilin University, Changchun, 130012, China
2. Institute for Applied Materials, Karlsruhe Institute of Technology, Hermann-von-Helmholtz-Platz 1, D-76344 Eggenstein-Leopoldshafen, Germany
3. Mohammed VI Polytechnic University (UM6P), Lot 660 – Hay Moulay Rachid, 43150 Benguerir, Morocco.
E-mail: wangyizhan@jlu.edu.cn; qiang.fu@kit.edu

**Abstract** The simultaneous intercalation of protons and $Zn^{2+}$ ions in aqueous electrolytes presents a significant obstacle to the widespread adoption of aqueous zinc ion batteries (AZIBs) for large-scale use, a challenge that has yet to be overcome. To address this, we have developed a $MnO_2$/tetramethylammonium (TMA) superstructure with an enlarged interlayer spacing, designed specifically to control $H^+$/$Zn^{2+}$ co-intercalation in AZIBs. Within this superstructure, the pre-intercalated $TMA^+$ ions work as spacers to stabilize the layered structure of $MnO_2$ cathodes and expand the interlayer spacing substantially by 28% to 0.92 nm. Evidence from *in operando* pH measurements, *in operando* synchrotron X-ray diffraction, and X-ray absorption spectroscopy shows that the enlarged interlayer spacing facilitates the diffusion and intercalation of $Zn^{2+}$ ions (which have a large ionic radius) into the $MnO_2$ cathodes. This spacing also helps suppress the competing $H^+$ intercalation and the formation of detrimental $Zn_4(OH)_6SO_4\cdot5H_2O$, thereby enhancing the structural stability of $MnO_2$. As a result, enhanced $Zn^{2+}$ storage properties, including excellent capacity and long cycle stability, are achieved.

**Keywords**: aqueous zinc ion batteries, $MnO_2$, superstructure, in operando synchrotron diffraction, X-ray absorption spectroscopy

## Introduction

Recently, aqueous zinc ion batteries (AZIBs) with mildly acidic electrolytes are gaining considerable attention for large-scale energy storage due to the high theoretical capacity of the zinc metal anode, as well as their environmental friendliness, easy fabrication, and low cost.[1-3] Meanwhile, manganese oxide ($MnO_2$) materials are particularly desirable for use as cathodes for AZIBs due to their high working voltage, high specific capacity, abundance, affordability, easy processing, and eco-friendliness.[4] Despite this, recent studies have demonstrated that a significant amount of $H^+/Zn^{2+}$ co-insertion occurs when $MnO_2$ cathodes are cycled using inexpensive $ZnSO_4$ electrolytes, which are the electrolytes of choice for large-scale energy storage applications.[5-13] The intercalation of $H^+$ in mildly acidic aqueous $ZnSO_4$ electrolytes (i.e. 2 M $ZnSO_4$, pH ≈ 4) induces the formation of $Zn_4(OH)_6SO_4 \cdot xH_2O$ (ZHS). This process leads to the formation of an insulating layer on the electrode surface, which then detaches from the electrode during cycling, leading to active material loss and eventual cell failure.[14-16] Moreover, because the concentration of $H^+$ is much lower than that of $Zn^{2+}$ in the mildly acidic aqueous electrolytes, the intercalation of $H^+$ promotes disassociation of water in electrolytes[17-20] and induces the collapse of the $MnO_2$ host lattice during repeated cycling.[21] Therefore, controlling the $H^+/Zn^{2+}$ co-intercalation in aqueous media is vital for developing high-performance cathode materials in AZIBs.

Limited approaches have been reported to mitigate the detrimental $H^+$ intercalation and enhance $Zn^{2+}$ intercalation in aqueous electrolytes.[22] Important advances in this direction include regulating water activity[15], tuning the zinc ion solvation structure[14], and subfreezing the batteries[22], etc. The interlayer spacing of $MnO_2$ is expected to be a critical factor in the competition between $Zn^{2+}$ and $H^+$ intercalation at the interface of $MnO_2$, due to their distinct differences in ionic radius. Compared to $H^+$, the ionic radius and atomic weight of $Zn^{2+}$ are larger, resulting in slower kinetics for $Zn^{2+}$ intercalation.[23-26] To effectively address the issue of low $Zn^{2+}$ diffusion and intercalation rates in $MnO_2$ cathodes, it is essential to provide enough space to accommodate $Zn^{2+}$ and its solvation sheath (approximately. 0.86 nm),[27] a challenge that remains.

Herein, we demonstrate a $MnO_2$/tetramethylammonium (TMA) superstructure (TMA-$MnO_2$) with an enlarged interlayer spacing as a stable cathode for AZIBs. In the superstructure, the pre-intercalated TMA cations act as spacers to stabilize the layered structure of the $MnO_2$ and substantially expand the interlayer spacing to 0.92 nm, which facilitates the diffusion of $Zn^{2+}$ in the $MnO_2$ cathode and increases the number of active sites. *In operando* techniques including pH characterizations, synchrotron X-ray diffraction and X-ray absorption spectroscopy (XAS) were performed to study the energy storage mechanism of TMA-$MnO_2$ during cycling. These studies show that the enlarged interlayer spacing can effectively enhance the intercalation of $Zn^{2+}$ and restrict the competing $H^+$ intercalation, which helps suppress the concomitant deposition of ZHS and improve the structure stability of $MnO_2$. As a result, the TMA-$MnO_2$ superstructure cathode exhibits enhanced charge-discharge performance, including excellent capacity and long cycle stability, holding great promise for the development of advanced cathode materials in AZIBs.

## 2. Experimental section

### 2.1. Materials

$KMnO_4$ (Analytical Reagent (AR), 99.5%), and $H_2SO_4$ (AR, 98%) were purchased from Beijing Chemical Works. $N(CH_3)_4Cl$ (99%) was purchased from Innochem. Super P was obtained from Sigma-Aldrich. Polyvinylidene difluoride (PVDF) (Solef® 5130) was purchased from Arkema. $CH_3OH$ (AR, 99.5%), $CH_3CH_2OH$ (AR, 97%), $ZnSO_4 \cdot 7H_2O$ (AR, 99.7%), $MnSO_4 \cdot H_2O$ (AR, 99%), and N-Methyl-2-pyrrolidone (NMP) (AR, 99.9%) were purchased from Aladdin. All chemicals and solvents were used as received.

### 2.2. Synthesis of materials

***Synthesis of $MnO_2$*:** A mixture of $KMnO_4$ (0.75 mmol), $H_2SO_4$ (0.75 mmol), and $CH_3OH$ (15 mmol) was combined in 500 mL of water and stirred for 10 minutes. The solution was then heated at 95°C for 1 hour, resulting in the formation of a $MnO_2$ nanosheet suspension. The pristine $MnO_2$ material was isolated through centrifugation, followed by multiple washes with deionized water and ethanol. It was subsequently dried at 60°C under vacuum for 12 hours.

***Synthesis of TMA-$MnO_2$*:** To the aforementioned $MnO_2$ nanosheet suspension, a 0.5 M solution of tetramethylammonium chloride (TMA, 50 mL) was added and stirred for 1 hour. The precipitate was separated via centrifugation and washed repeatedly with deionized water and ethanol. The TMA-$MnO_2$ product was then dried at 60°C under vacuum for 12 hours.

### 2.3. Material Characterization

The X-ray diffraction (XRD) patterns of $MnO_2$ were collected using a Bruker D8 equipped with Cu K$\alpha$-radiation. The scanning electron microscopy (SEM) and energy dispersive spectroscopy (EDS) analyses were performed on a Hitachi Regulus8100. A JEM-2200FS from JEOL was used for transmission electron microscopy (TEM) measurement. X-ray photoelectron spectroscopy (XPS) was recorded using a Thermo Scientific NEXSA. Fourier-transform infrared spectroscopy (FTIR) was performed using a VERTEX 80V. Thermogravimetric analysis (TGA) was measured with a STA 449F3 from NETZSCH in an air atmosphere. The *in operando* pH values were measured with a Mettler Toledo-FE28 equipped with an Inlab microprobe.

### 2.4. Electrochemical Measurements

The 2032-type coin cells were assembled with $MnO_2$/TMA-$MnO_2$ as the cathode, Zn foil as the anode, and a 2 M $ZnSO_4$ + 0.2 M $MnSO_4$ aqueous solution as the electrolyte. The initial pH of the electrolyte was adjusted to around 5.1 using a trace amount of ZnO. The cathodes were prepared by mixing the $MnO_2$/TMA-$MnO_2$ (60 wt%), Super P (30 wt%), and PVDF (10 wt%) with NMP to form a slurry, which was then cast on the titanium foil. The mass loading of active materials was approximately 1.2 mg $cm^{-2}$. The cyclic voltammetry (CV) tests were performed on a Bio-Logic VSP multichannel electrochemical workstation. The galvanostatic charge/discharge curves (GCD), cycling performance, and galvanostatic intermittent titration technique (GITT) were measured using a LAND-2010 automatic battery tester. The three-electrode test was carried out with a carbon rod as the counter electrode, Ag/AgCl as the reference electrode, and $MnO_2$/TMA-$MnO_2$ as the working electrode.

### 2.5 In operando synchrotron-based experiments

A modified 2025-type coin cell was used with a 5-mm hole in the center of both the cathode and anode. The mass loading of $MnO_2$ in the cathode was ~5.0 mg·$cm^{-2}$. *In operando* synchrotron diffraction was performed using synchrotron radiation (λ=0.20734 Å, 60 keV) at the P02.1 beamline PETRA, DESY in Hamburg. Current densities of 20 mA

$g^{-1}$ for $MnO_2$ and 25 mA $g^{-1}$ for TMA-$MnO_2$ were used for the first cycles between 1.8 V and 0.8 V and also for *in operando* X-ray absorption spectroscopy (XAS) at the P65 beamline at PETRA. The Mn K-edge XAS spectra were recorded in quick-XAS (5 min/spectrum) mode in fluorescence geometry using a passivated implanted planar silicon (PIPS) diode detector. The Mn K-edges for $MnO_2$ and TMA-$MnO_2$ were measured during electrochemical cycling, and the energies were calibrated using a Mn foil as commonly employed in XAS experiments. $MnO_2$, $Mn_2O_3$, and MnO were used as standard materials. All the XAS data were collected at room temperature with a Si(111) double-crystal monochromator, and all the XAS spectra were analyzed and processed utilizing the DEMETER software package.

### *2.6 In operando pH measurement*

The pH evolution on the cathode region was measured with an H-type cell, as shown in **Figure S6**. The Zn anode and cathode with the same size of 2.5 cm × 3.5 cm were placed at opposite sides of an H-cell. Then the 2 M $ZnSO_4$ + 0.2 M $MnSO_4$ aqueous electrolyte was added. The micro probe of the pH meter was then placed near to the cathode region. In-situ pH tests were carried out with a current density of 100 mA $g^{-1}$ between 1.8 V and 0.8 V.

## 3. Results and Discussion

The TMA-$MnO_2$ material was prepared by a bottom-up self-assembly of $MnO_2$ nanosheets and TMA cations, as illustrated in **Figure 1a**. The effect of TMA pre-intercalation on the crystal structure and layer spacing was demonstrated by XRD (**Figure 1b**). The strongest reflections of pristine $MnO_2$ can be found at 12.3°, 24.8°, 36.6°, and 65.7°, which are indexed to the (001), (002), (110), and (020) planes of layered birnessite $MnO_2$ ($K_{0.46}Mn_2O_4\cdot(H_2O)_{1.6}$, JCPDS: 01-080-1098) with *C2/m* symmetry and lattice parameters of a = 5.15 Å, b = 2.84 Å, c = 7.18 Å, and $\beta$=100.76°. For TMA-$MnO_2$, the corresponding reflections are located at 9.8°, 18.3°, 36.6°, and 65.7°. Notably, the Bragg reflection 001 shifts from 12.3° to 9.8°, corresponding to an expansion of the interlayer spacing in the c-axis direction from 0.72 nm to 0.92 nm, which indicates that TMA was uniformly intercalated into the interlayer of $MnO_2$, forming a superstructure. The enlarged interlayer spacing enhances ionic conductivity and supports the (de)insertion of $Zn^{2+}$ ions, further improving the storage capacity of $MnO_2$, as demonstrated in the subsequent sections. Moreover, after TMA intercalation, the 110 and 020 reflections show no shift with respect to pristine $MnO_2$, indicating that the in-plane lattices of $MnO_2$ remain unchanged. The morphology and interlayer spacing of both pristine $MnO_2$ and TMA-$MnO_2$ were further characterized by SEM and HRTEM (**Figure S1**). As indicated in **Figure S2**, the SEM images of both TMA-$MnO_2$ and pristine $MnO_2$ exhibit a distinctive nano-flower morphology, which is assembled from two-dimensional nanosheets. This nano-flower structure is notable because it provides a high surface area and facilitates efficient ion transport. As shown in **Figure 1c**, the measured interlayer spacing of TMA-$MnO_2$ in the HRTEM image is 0.91 nm, which is 0.20 nm larger than that of pristine $MnO_2$ (0.71 nm). Both spacing values align well with the XRD results, further validating the successful intercalation of TMA into the interlayer of $MnO_2$ and the consequent enlargement of the interlayer spacing. TGA and FTIR spectra were then carried out to further understand the detailed structure of TMA-$MnO_2$. As shown in the TGA curves (**Figure 1e**), the weight loss before 200°C is attributed to the removal of physically absorbed water, while the weight loss between 200 to 350°C results from the thermal decomposition of TMA and structural water. Based on the different pyrolysis temperatures of the components, the weight ratio of TMA in TMA-$MnO_2$ is identified as ~5.5%. The FTIR spectra for TMA, pristine $MnO_2$, and TMA-$MnO_2$ are shown in **Figure 1f**. The characteristic peak of Mn-O stretching vibration is observed in both pristine $MnO_2$ (505 $cm^{-1}$) and TAM-$MnO_2$ (498 $cm^{-1}$). In addition, the characteristic vibration peaks[28] of $C_4N$ at 948 $cm^{-1}$, $CH_3$ group at 1487 $cm^{-1}$, and C-H at 2922 $cm^{-1}$ are found in TMA-$MnO_2$, suggesting the existence of TMA in the material. Furthermore, the elemental composition of TMA-$MnO_2$ was studied by XPS and EDS. As shown in the XPS spectra (**Figure 1g)**, besides Mn and O, the unique N element from TMA is observed in TMA-$MnO_2$. The N 1s XPS located at 401.83 eV originates from the ammonium group in TMA. Both Mn 3s and Mn 2p XPS spectra indicate a slight reduction in the Mn valence state induced by $TMA^+$ intercalation **(Figure S3a-b)**. Meanwhile, the O 1s XPS spectra show a reduction in the crystalline water content in TMA-$MnO_2$ (**Figure S3c**). The EDS mapping images show that N, Mn, and O elements are uniformly dispersed in the TMA-$MnO_2$ nanosheets, indicating the homogeneous distribution of TMA (**Figure 1d**).

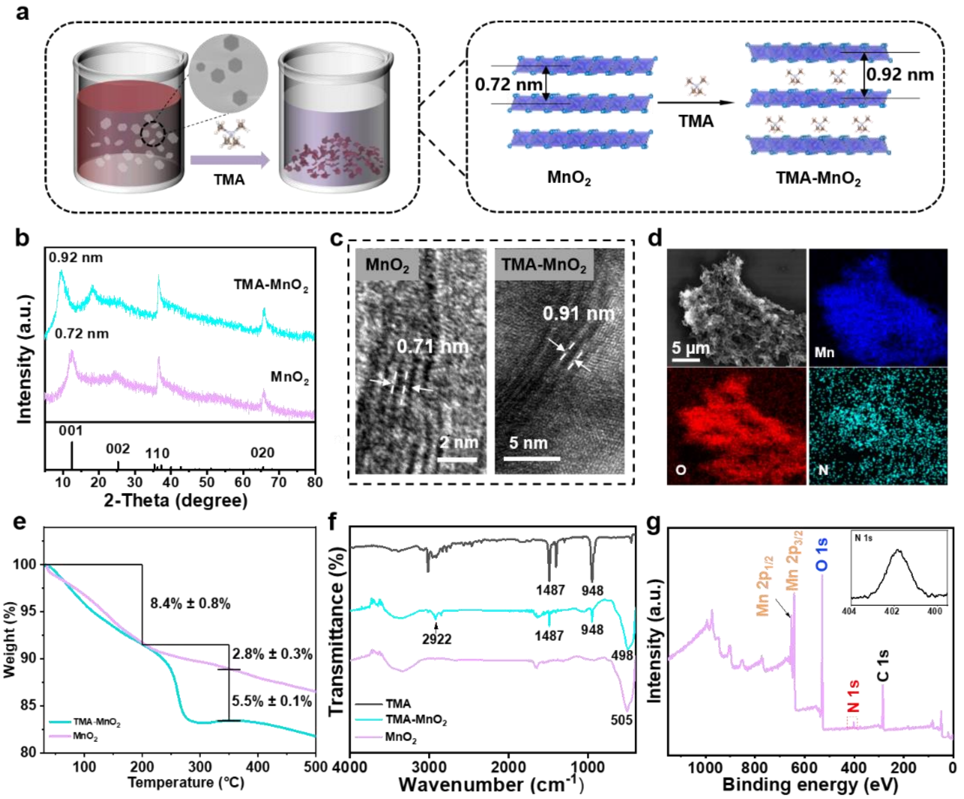

**Figure 1. a**), Schematic illustration of the preparation of TMA-$MnO_2$; **b**), XRD patterns of $MnO_2$ and TMA-$MnO_2$ (Cu Kα); **c**), HRTEM images of $MnO_2$ and TMA-$MnO_2$; **d**), SEM image and the corresponding EDS mapping of TMA-$MnO_2$; **e**), TGA of the TMA-$MnO_2$ and $MnO_2$. The error estimates are provided based on the precision of one experiment; **f**), FTIR spectra of TMA, $MnO_2$, and TMA-$MnO_2$; **g**), The XPS spectra of TMA-$MnO_2$ and the corresponding high-resolution N 1s (inset).

The electrochemical performance of TMA-$MnO_2$ and $MnO_2$ cathodes in AZIBs was studied with coin cells using a 2 M $ZnSO_4$ + 0.2 M $MnSO_4$ aqueous electrolyte. The first three CV curves were collected at a scan rate of 0.27 mV $s^{-1}$ (equivalent to 1 C) over the voltage range of 0.8 V to 1.8 V (**Figure 2a-b**). Two pairs of redox peaks are observed for both TMA-$MnO_2$ and $MnO_2$ in AZIBs, indicating that both materials undergo a two-step electrochemical process. Irreversible processes are observed in the first cycle for both cathodes. In subsequent cycles, the CV curves retain their shapes, demonstrating the good reversibility of the redox reactions. Notably, compared to $MnO_2$, TMA-$MnO_2$ shows a lower overpotential (0.292 V vs 0.330 V). Furthermore, the sharper oxidation peak and high current response in TMA-$MnO_2$ compared to $MnO_2$ indicates a faster ion migration rate within the TMA-$MnO_2$ structure. The pre-embedding of $TMA^+$ ions into the interlayers of $MnO_2$ enhances the reaction kinetics by improving ion diffusion pathways. The enhanced ion diffusion coefficient for the TMA-$MnO_2$ electrodes was further confirmed by GITT (**Figure S4**). EIS spectra also imply that the TMA-$MnO_2$ electrode possesses a lower interface charge transfer resistance (**Figure S5**). **Figure 2c** presents the rate performance of the TMA-$MnO_2$ and $MnO_2$ cathodes. As the current density increases, the specific capacity decreases for both cathodes. At a low current density of 0.05 A $g^{-1}$, the TMA-$MnO_2$ cathode exhibits an average capacity of 319 mAh $g^{-1}$. When the current density increases to 3 A $g^{-1}$, a specific capacity of 136 mAh $g^{-1}$ is retained. In contrast, the $MnO_2$ cathode only delivers an average capacity of 230 mAh $g^{-1}$ at 0.05 A $g^{-1}$ and 129 mAh $g^{-1}$ at 3 A $g^{-1}$. Note that TMA-$MnO_2$ shows a larger capacity decrease as the current density increases. This might suggest that under high current density, the dominant inserted ion type changes, resulting in a significant reduction in the capacity. A more detailed discussion of the energy storage mechanism is presented in the following sections. GCD tests were performed to investigate the cycling stability of the cells. As shown in **Figure 2d**, the TMA-$MnO_2$ cell exhibits a discharge capacity of 298 mAh $g^{-1}$ at 0.5 A $g^{-1}$, which is 1.3 times larger than that of $MnO_2$ (222 mAh $g^{-1}$). After 200 cycles, the specific capacity for TMA-$MnO_2$ can still reach 263 mAh $g^{-1}$ with 88% capacity retention, which is more stable than that of $MnO_2$ (**Figure 2e**). In addition, the TMA-$MnO_2$ cell still performs excellently at a high current density of 1 A $g^{-1}$, maintaining 205 mAh $g^{-1}$ after 500 cycles (**Figure 2f**). In contrast, the capacity of $MnO_2$ quickly drops to 60 mAh $g^{-1}$ after 500 cycles. TMA-$MnO_2$ exhibits higher capacity, better rate performance, and a more stable cycling life compared with recently reported Zn||$MnO_2$ batteries (**Table S1**). [29-42]

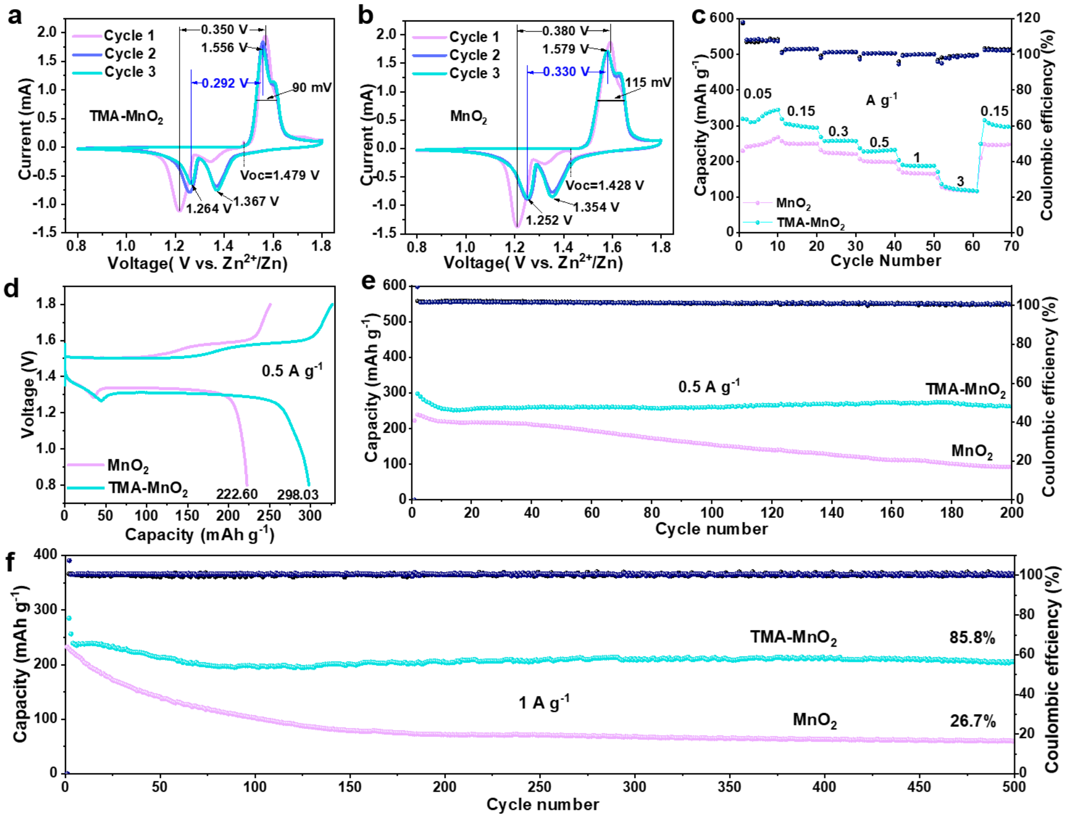

**Figure 2.** CV curves of **a**) TMA-MnO$_2$ and **b**) MnO$_2$ at 0.27 mV s$^{-1}$; **c**), Rate performance of the TMA-MnO$_2$ and MnO$_2$ electrodes; **d**), GCD curves of TMA-MnO$_2$ and MnO$_2$ at 0.5 A g$^{-1}$; Cycling performance of TMA-MnO$_2$ and MnO$_2$ at current densities of **e**) 0.5 A g$^{-1}$ and **f**) 1 A g$^{-1}$.

*In operando* synchrotron diffraction was performed to illustrate the phase evolution of TMA-MnO$_2$ and MnO$_2$ during the discharge/charge processes (**Figure 3**). For the MnO$_2$ electrode, the synchrotron diffraction patterns show reflections at 1.67°, 4.85°, and 8.40°. These reflections correspond to the (001), (110), and (020) crystal planes of MnO$_2$ respectively, similar to what is typically observed in XRD spectra. For the TMA-MnO$_2$ electrode, synchrotron diffraction patterns display reflections at 4.86° and 8.41°, corresponding to the (110) and (020) crystal planes. Bragg reflections at 1.08°, 1.66°, 4.35°, 4.83°, 7.53°, and 8.37° are observed for both MnO$_2$ and TMA-MnO$_2$ during discharging to 0.8 V. These reflections correspond to the formation of the $Zn_4(OH)_6SO_4\cdot 5H_2O$ by-product (ZHS, JCPDS No. 78-0246) with space group $P\bar{1}$ and lattice parameters a = 8.354 Å, b=8.350 Å, c=11.001 Å, and $\alpha$ = 94.41°, $\beta$= 82.95°, $\gamma$= 119.93°. Especially, the 001 reflection, with a large interplanar spacing of ~11 Å, exhibits extremely high intensity at the end of discharge, suggesting a preferential growth of ZHS byproduct along [001] direction. After charging back to 1.8 V, the ZHS reflections completely disappear. Note that the Bragg reflections of $MnO_2$ are well maintained throughout the initial discharge/charge cycle, indicating the structural robustness. For both electrodes, no reflections of spinel $ZnMn_2O_4$ or MnOOH can be observed, which indicates the good structure stability of the $MnO_2$ and TMA-$MnO_2$ cathodes. Generally, the insertion of $H^+$ into the cathode could increase the pH at the cathode region, resulting in ZHS precipitation.[10,16] Interestingly, the formation of ZHS appears later for TMA-$MnO_2$ than for $MnO_2$ electrodes, suggesting that less $H^+$ is inserted into TMA-$MnO_2$ than into $MnO_2$ during the first discharge. Moreover, a smaller amount of ZHS is formed on the TMA-$MnO_2$ electrode than on the $MnO_2$ electrode at the fully discharged state of 0.8 V, as concluded from the much lower intensity of the ZHS 001 reflection relative to the cathode reflections (**Figure 3c-d**).

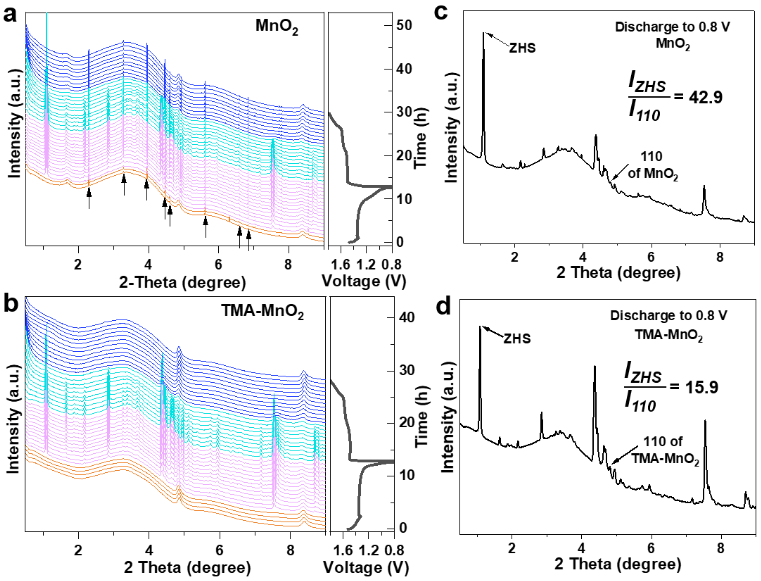

**Figure 3.** *In operando* synchrotron diffraction patterns (λ=0.20734 Å, 60 keV) of **a**) $MnO_2$ and **b**) TMA-$MnO_2$ electrodes for the 1st discharge and charge cycle. The marked reflections in **a**) are from the test cells and do not shift for different states of charge and discharge. The corresponding diffraction patterns for the fully discharged state (0.8 V) of **c**) $MnO_2$ and **d**) TMA-$MnO_2$.

To further explore the ion intercalation mechanisms of $MnO_2$ and TMA-$MnO_2$, *in operando* pH changes at the cathode interface-near region of AZIB using the 2 M $ZnSO_4$ + 0.2 M $MnSO_4$ electrolyte were measured (**Figure 4a-b and S6**). During the discharge process, the pH value at the $MnO_2$ electrode surface increases gradually (**Figure 4a**), indicating that $H^+$ ions insert into the cathode, thus leading to a decrease of the $H^+$ concentration at the cathode interface-near region. Notably, a sudden drop of pH from 5.26 to 5.10 happens at the beginning of the charge, indicating some $H^+$ ions are extracted from the discharged cathode. During the subsequent charging process, the pH value at the cathode region decreases gradually, indicating the continuous $H^+$ release from the cathode. Interestingly, a different pH change behavior is observed for the TMA-$MnO_2$ electrode. As shown in **Figure 4b**, during the discharge process, the pH value at the TMA-$MnO_2$ electrode region initially decreases, then increases. A sudden pH increase is observed at the beginning of the charging process, suggesting that much fewer $H^+$ ions are released from the cathode compared to the $MnO_2$ electrode. During the further charging process, the pH value at the TMA-$MnO_2$ electrode region shows a decrease-increase-decrease pattern. These fluctuations in pH value for TMA-$MnO_2$ during the discharge and charge process are probably related to the more competitive $Zn^{2+}$ (de)intercalation. Compared to the $MnO_2$ electrode, the TMA-$MnO_2$ electrode exhibits a smaller total decrease in pH value during the charging process, providing further evidence of reduced $H^+$ release from the TMA-$MnO_2$ electrode.

To further confirm the promoted $Zn^{2+}$ insertion mechanism, the electrochemical behaviors of the $MnO_2$ and TMA-$MnO_2$ electrodes were compared in 0.2 M $MnSO_4$ electrolytes with or without 2 M $Zn^{2+}$ using the three-electrode cells, as shown in **Figure 4c**. The TMA-$MnO_2$ electrode in the $Zn^{2+}$ containing electrolyte shows a larger discharge capacity of 286 mAh $g^{-1}$ at 0.1 A $g^{-1}$ compared to $MnO_2$ (237 mAh $g^{-1}$), aligning with observations from two-electrode coin cells (**Figure 2c**). In the electrolyte without $Zn^{2+}$, the discharge capacities of TMA-$MnO_2$ and $MnO_2$ decrease to 210 and 208 mAh $g^{-1}$, respectively, indicating that $H^+$ insertion takes place. The TMA-$MnO_2$ and $MnO_2$ have similar capacities with only $H^+$ insertion, demonstrating a larger amount of competitive $Zn^{2+}$ insertion for TMA-$MnO_2$ in the $Zn^{2+}$-containing electrolytes. To provide additional insights, we conducted experiments utilizing a non-protonic electrolyte of 2 M $ZnSO_4$ +

0.2 M $MnSO_4$ in dimethyl sulfoxide (DMSO) (**Figure S7**). The discharge profiles of both materials exhibited a single, continuous $Zn^{2+}$ insertion behavior. Remarkably, TMA-$MnO_2$ demonstrated a higher discharge specific capacity of 246.2 mAh $g^{-1}$ compared to $MnO_2$ (190.1 mAh $g^{-1}$) under the same conditions, indicating a greater $Zn^{2+}$ insertion capacity in TMA-$MnO_2$. Furthermore, the enhanced $Zn^{2+}$ insertion is further verified by EDS elemental mapping. The TMA-$MnO_2$ maintains its 2D morphology even after discharge (**Figure S8**) and the distribution of Mn, O, and N elements remains uniform within the sample, indicating the structural integrity and stability. The discharge electrode exhibits a uniform distribution of Zn elements, indicating the insertion of $Zn^{2+}$. Quantification from EDS analysis suggests a higher Zn/Mn atomic ratio for TMA-$MnO_2$ compared to $MnO_2$ (**Figure 4d and S9**).

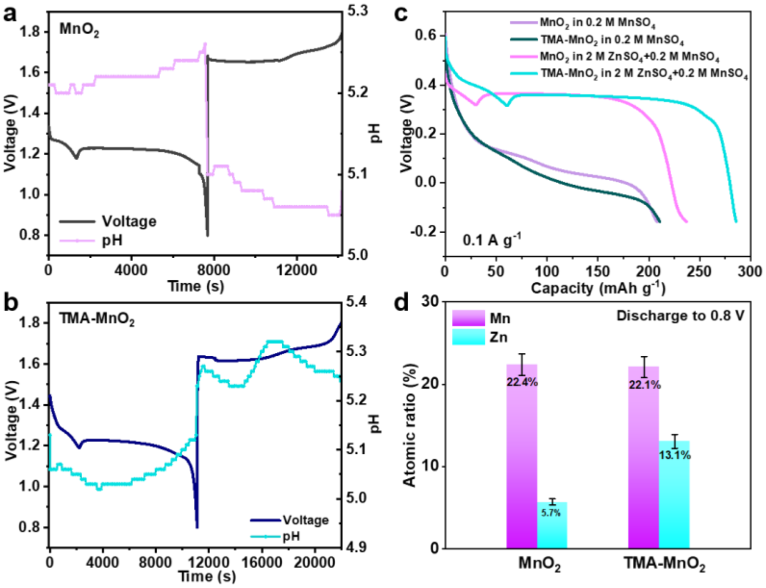

**Figure 4.** *In operando* pH change at **a**) $MnO_2$ and **b**) TMA-$MnO_2$ electrode interface-near region for the 1st discharge and charge cycle; **c**), Discharge curves of $MnO_2$ and TMA-$MnO_2$ electrode in 0.2 M $MnSO_4$ solution with and without 2 M $ZnSO_4$ as electrolytes at 0.05 A $g^{-1}$ in a three-electrode cell with an Ag/AgCl electrode as reference and Pt metal as counter electrode; **d**), The atomic ratios of Mn and Zn in the discharged $MnO_2$ and TMA-$MnO_2$ electrode. The error estimates are provided based on the precision of one experiment.

Furthermore, *in operando* XAS was performed to reveal changes in the electronic structure and coordination environment of the Mn redox centers during the electrochemical processes (**Figure 5** and **S10**). The Mn oxidation states were explored by X-ray absorption near-edge structure (XANES) analysis. During the discharge process, the Mn K-edge and pre-edge peaks shift towards lower energy, indicating a decrease in the average valence state of Mn in TMA-$MnO_2$. This is accompanied by a reduction in the intensity of the weak pre-edge peak, which is attributed to the decreased probability of transitions from the 1s into unoccupied 3d orbitals, partially allowed only due to electric quadrupole coupling and/or 3d-4p orbital mixing within the distorted $MnO_6$ octahedral framework. Note that the split in the pre-edge peaks arises from the separation of the degenerated 3d levels under an octahedral crystal field.[43] Two broad peaks of edge resonance (B) simultaneously move to lower energy with a decrease of intensity, which is attributed to energy absorption by core electrons.[44] During the following charge process, the Mn K-edge position shifts back to higher energy, demonstrating the reversible reduction and oxidation of Mn. The Mn K-edge XANES of the fresh and fully recharged electrodes are almost the same (**Figure S11**), indicating the very good reversibility of structural and electronic changes during cycling.

The changes in the local structure of Mn during the electrochemical processes were analyzed based on the phase uncorrected Fourier transform (FT) ($k^3$-weighted) of the V K-edge extended X-ray absorption fine structure (EXAFS). The initial TMA-$MnO_2$ electrode shows peaks in the radial distribution centered at ~1.5 Å and 2.5 Å, corresponding to Mn-O and Mn-Mn distances, respectively.[45] During discharge, the FT amplitudes for both Mn-O and Mn-Mn distances decrease, attributed to the local structure distortion resulting from Jahn-Teller distortion associated with the reduction of the Mn oxidation state accompanied by the insertion of ions.[46,47] Compared to the EXAFS spectrum of $MnO_2$, the amplitude decrease in TMA-$MnO_2$ was much larger, indicating larger local structure distortions in the TMA-$MnO_2$ electrode. The FT peaks for $MnO_2$ show no shift during discharge. In contrast, the FT peak shift is observed for TMA-$MnO_2$, probably due to more competitive $Zn^{2+}$ intercalation.[6,48] At the fully discharged state, the two characteristic FT peaks are preserved, suggesting the stable Mn-O network in TMA-$MnO_2$ during ions insertion. During the following charging process, the amplitudes, and positions of the FT peaks for

Mn-O and Mn-Mn bonds recover back to those of the fresh electrode (**Figure 5d**), further indicating good reversibility of the TMA-$MnO_2$ electrode with robust structure.

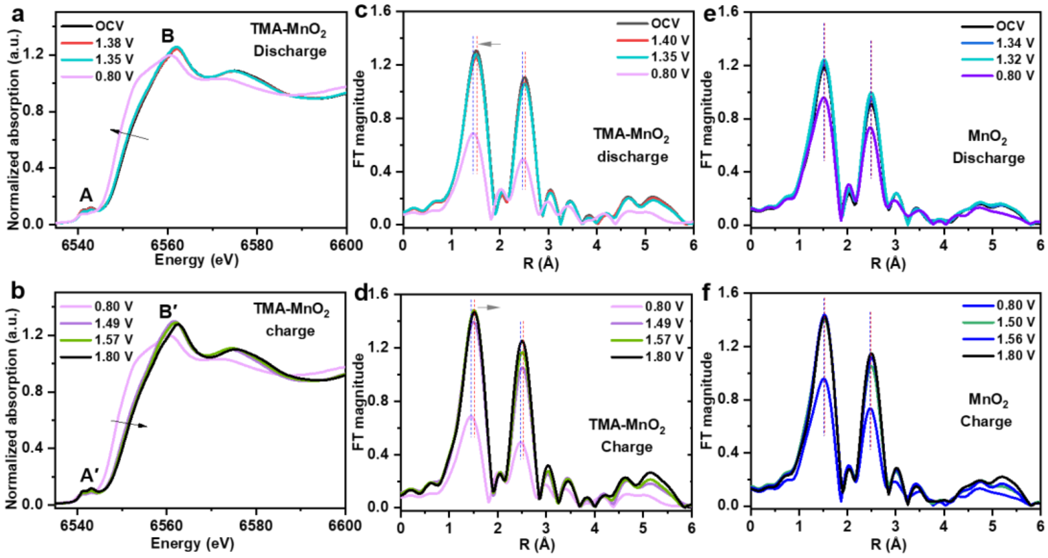

**Figure 5. a**), **b**) *In operando* Mn K-edge XANES spectra of TMA-$MnO_2$; Phase uncorrected Fourier transforms of Mn K-edge EXAFS ($k^3$-weighted) of **c**), **d**) TMA-$MnO_2$ electrode and **e**), **f**) $MnO_2$ electrode during the first discharge and charge cycle.

## Conclusion

This study introduces the novel development of a $MnO_2$/tetramethylammonium superstructure (TMA-$MnO_2$) as a cathode material for aqueous zinc-ion batteries (AZIBs). The intercalation of TMA significantly expands the interlayer spacing of the $MnO_2$ matrix, facilitating the diffusion and preferential intercalation of $Zn^{2+}$ ions into the $MnO_2$ cathodes. This structural modification has led to a marked improvement in electrochemical performance, including a higher specific discharge capacity of 298 mAh $g^{-1}$ at 0.5 A $g^{-1}$. Additionally, the cathode maintains a high capacity retention rate, delivering 263 mAh $g^{-1}$ after 200 cycles, corresponding to 88% capacity retention. Our innovative approach leverages in operando analysis to demonstrate how the TMA-$MnO_2$ superstructure effectively promotes $Zn^{2+}$ intercalation while simultaneously inhibiting competing $H^+$ intercalation. This dual function not only enhances the battery's performance but also mitigates the formation of the by-product zinc hydroxysulfate (ZHS), thereby enhancing the structural stability of the $MnO_2$. Compared to existing literature, our TMA-$MnO_2$

cathodes show significant improvements over traditional $MnO_2$ electrodes, which typically exhibit lower $Zn^{2+}$ storage capacities and stability. For instance, Li et al. (ref 29) have reported maximum capacities around 195 mAh $g^{-1}$ at 0.3 A $g^{-1}$ and rapid capacity fading to 113 mAh $g^{-1}$ within 100 cycles for similar systems. Similarly, Xie et al. (ref 31) found maximum capacities of around 150 mAh $g^{-1}$ at 2.0 A $g^{-1}$ with capacity fading to 80 mAh $g^{-1}$ within 200 cycles. Our approach not only surpasses these metrics but also addresses common challenges associated with ion co-intercalation. We envision further exploring the underlying mechanisms of ion intercalation and transport within layered structures like TMA-$MnO_2$. We aim to synthesize and test other organic cation intercalated variants to broaden the applicability of this strategy to other types of rechargeable batteries. Additionally, scaling up this technology for commercial applications and optimizing the synthesis process to enhance the eco-friendliness and cost-effectiveness of the production are among our top priorities.

## Acknowledgements

Aina Zhang and Xu Zhang contributed equally to this work. This work was supported by the National Natural Science Foundation of China (No. 22172061, 22279043), the Fundamental Research Funds for the Central Universities, Instrument and equipment sharing platform, College of physics, Jilin University. This work contributes to the research performed at CELEST (Center for Electrochemical Energy Storage Ulm-Karlsruhe) and was partially funded by the German Research Foundation (DFG) under Project ID 390874152 (POLiS Cluster of Excellence). We acknowledge DESY (Hamburg, Germany), a member of the Helmholtz Association HGF, for the provision of experimental facilities. Parts of this research were carried out at PETRA III beamlines P02.1 and P65, DESY, Hamburg, Germany. Beamtime was allocated for proposal(s) I-20211296 and I-20211294. We express our thanks to Dr. Volodymyr Baran and Dr. Edmund Welter from DESY. The *in operando* XAS work was performed using the Biologic potentiostat of PETRA III beamline P02.1.

## References

[1] Zhu, Z.;Jiang, T.;Ali, M.;Meng, Y.;Jin, Y.;Cui, Y.;Chen, W. Rechargeable Batteries for Grid Scale Energy Storage. *Chem. Rev.* **2022**, *122*, 16610-16751.

[2] Ruan, P.;Liang, S.;Lu, B.;Fan, H. J.;Zhou, J. Design Strategies for High-Energy-Density Aqueous Zinc Batteries. *Angew. Chem. Int. Ed.* **2022**, *61*, e202200598.

[3] Li, C.;Jin, S.;Archer, L. A.;Nazar, L. F. Toward practical aqueous zinc-ion batteries for electrochemical energy storage. *Joule* **2022**, *6*, 1733-1738.

[4] Li, J.;Luo, N.;Kang, L.;Zhao, F.;Jiao, Y.;Macdonald, T. J.;Wang, M.;Parkin, I. P.;Shearing, P. R.;Brett, D. J. L.;Chai, G.;He, G. Hydrogen-Bond Reinforced Superstructural Manganese Oxide As the Cathode for Ultra-Stable Aqueous Zinc Ion Batteries. *Adv. Energy Mater.* **2022**, 2201840.

[5] Cui, G.;Zeng, Y.;Wu, J.;Guo, Y.;Gu, X.;Lou, X. W. D. Synthesis of Nitrogen-Doped $KMn_8O_{16}$ with Oxygen Vacancy for Stable Zinc-Ion Batteries. *Adv. Sci.* **2022**, *9*, e2106067.

[6] Zhu, X.;Cao, Z.;Wang, W.;Li, H.;Dong, J.;Gao, S.;Xu, D.;Li, L.;Shen, J.;Ye, M. Superior-Performance Aqueous Zinc-Ion Batteries Based on the In Situ Growth of MnO2 Nanosheets on $V_2CT_X$ MXene. *ACS Nano* **2021**, *15*, 2971-2983.

[7] Zhao, Y.;Zhang, P.;Liang, J.;Xia, X.;Ren, L.;Song, L.;Liu, W.;Sun, X. Uncovering sulfur doping effect in $MnO_2$ nanosheets as an efficient cathode for aqueous zinc ion battery. *Energy Storage Mater.* **2022**, *47*, 424-433.

[8] Tang, H.;Chen, W.;Li, N.;Hu, Z.;Xiao, L.;Xie, Y.;Xi, L.;Ni, L.;Zhu, Y. Layered $MnO_2$ nanodots as high-rate and stable cathode materials for aqueous zinc-ion storage. *Energy Storage Mater.* **2022**, *48*, 335-343.

[9] Zhao, Y.;Zhou, R.;Song, Z.;Zhang, X.;Zhang, T.;Zhou, A.;Wu, F.;Chen, R.;Li, L. Interfacial Designing of $MnO_2$ Half-Wrapped by Aromatic Polymers for High-Performance Aqueous Zinc-Ion Batteries. *Angew. Chem. Int. Ed.* **2022**, *61*, e202212231.

[10] Sambandam, B.;Mathew, V.;Kim, S.;Lee, S.;Kim, S.;Hwang, J. Y.;Fan, H. J.;Kim, J. An analysis of the electrochemical mechanism of manganese oxides in aqueous zinc batteries. *Chem* **2022**, *8*, 924-946.

[11] Chen, H.;Dai, C.;Xiao, F.;Yang, Q.;Cai, S.;Xu, M.;Fan, H. J.;Bao, S. J. Reunderstanding the Reaction Mechanism of Aqueous Zn-Mn Batteries with Sulfate Electrolytes: Role of the Zinc Sulfate Hydroxide. *Adv. Mater.* **2022**, *34*, e2109092.

[12] Sun, W.;Wang, F.;Hou, S.;Yang, C.;Fan, X.;Ma, Z.;Gao, T.;Han, F.;Hu, R.;Zhu, M.;Wang, C. Zn/$MnO_2$ Battery Chemistry With $H^+$ and $Zn^{2+}$ Coinsertion. *J. Am. Chem. Soc.* **2017**, *139*, 9775-9778.

[13] Huang, J.;Wang, Z.;Hou, M.;Dong, X.;Liu, Y.;Wang, Y.;Xia, Y. Polyaniline-intercalated manganese dioxide nanolayers as a high-performance cathode material for an aqueous zinc-ion battery. *Nat. Commun.* **2018**, *9*, 2906.

[14] Li, C.;Kingsbury, R.;Zhou, L.;Shyamsunder, A.;Persson, K. A.;Nazar, L. F. Tuning the Solvation Structure in Aqueous Zinc Batteries to Maximize Zn-Ion Intercalation and Optimize Dendrite-Free Zinc Plating. *ACS Energy Lett.* **2022**, *7*, 533-540.

[15] Wang, F.;Blanc, L. E.;Li, Q.;Faraone, A.;Ji, X.;Chen-Mayer, H. H.;Paul, R. L.;Dura, J. A.;Hu, E.;Xu, K.;Nazar, L. F.;Wang, C. Quantifying and Suppressing Proton Intercalation to Enable High-Voltage Zn-Ion Batteries. *Adv. Energy Mater.* **2021**, *11*, 2102016.

[16] Oberholzer, P.;Tervoort, E.;Bouzid, A.;Pasquarello, A.;Kundu, D. Oxide versus Nonoxide Cathode Materials for Aqueous Zn Batteries: An Insight into the Charge Storage Mechanism and Consequences Thereof. *ACS Appl. Mater. Interfaces* **2019**, *11*, 674-682.

[17] Yuan, Y.;Sharpe, R.;He, K.;Li, C.;Saray, M. T.;Liu, T.;Yao, W.;Cheng, M.;Jin, H.;Wang, S.;Amine, K.;Shahbazian-Yassar, R.;Islam, M. S.;Lu, J. Understanding intercalation chemistry for sustainable aqueous zinc–manganese dioxide batteries. *Nat. Sustain.* **2022**, *5*, 890–898.

[18] Zhao, Q.;Song, A.;Zhao, W.;Qin, R.;Ding, S.;Chen, X.;Song, Y.;Yang, L.;Lin, H.;Li, S.;Pan, F. Boosting the Energy Density of Aqueous Batteries via Facile Grotthuss Proton Transport. *Angew. Chem. Int. Ed.* **2021**, *60*, 4169-4174.

[19] Zuo, Y.;Liu, P.;Ling, L.;Tian, M.;Wang, Z.;Tian, H.;Meng, T.;Sun, X.;Cai, S. Boosted $H^+$ Intercalation Enables Ultrahigh Rate Performance of the delta-$MnO_2$ Cathode for Aqueous Zinc Batteries. *ACS Appl. Mater. Interfaces* **2022**, *14*, 26653−26661.

[20] Zhang, Y.;Liu, Y.;Liu, Z.;Wu, X.;Wen, Y.;Chen, H.;Ni, X.;Liu, G.;Huang, J.;Peng, S. $MnO_2$ cathode materials with the improved stability via nitrogen doping for aqueous zinc-ion batteries. *J. Energy Chem.* **2022**, *64*, 23-32.

[21] Li, X.;Xu, Z.;Qian, Y.;Hou, Z. In-situ regulated competitive proton intercalation and deposition/dissolution reaction of $MnO_2$ for high-performance flexible zinc-manganese batteries. *Energy Storage Mater.* **2022**, *53*, 72-78.

[22] Gao, S.;Li, B.;Tan, H.;Xia, F.;Dahunsi, O.;Xu, W.;Liu, Y.;Wang, R.;Cheng, Y. High-Energy and Stable Subfreezing Aqueous Zn-$MnO_2$ Batteries with Selective and Pseudocapacitive Zn-Ion Insertion in $MnO_2$. *Adv. Mater.* **2022**, *34*, e2201510.

[23] Wang, S.;Yuan, Z.;Zhang, X.;Bi, S.;Zhou, Z.;Tian, J.;Zhang, Q.;Niu, Z. Non-Metal Ion Co-Insertion Chemistry in Aqueous Zn/$MnO_2$ Batteries. *Angew. Chem. Int. Ed.* **2021**, *60*, 7056 –7060.

[24] Blanc, L. E.;Kundu, D.;Nazar, L. F. Scientific Challenges for the Implementation of Zn-Ion Batteries. *Joule* **2020**, *4*, 771-799.

[25] Zhang, J.;Li, W.;Wang, J.;Pu, X.;Zhang, G.;Wang, S.;Wang, N.;Li, X. Engineering p-Band Center of Oxygen Boosting $H^+$ Intercalation in δ-$MnO_2$ for Aqueous Zinc Ion Batteries. *Angew. Chem. Int. Ed.* **2023**, *62*, e202215654.

[26] Zhang, H.;Wu, W.;Liu, Q.;Yang, F.;Shi, X.;Liu, X.;Yu, M.;Lu, X. Interlayer Engineering of α-$MoO_3$ Modulates Selective Hydronium Intercalation in Neutral Aqueous Electrolyte. *Angew. Chem. Int. Ed.* **2021**, *60*, 896-903.

[27] Zhu, K.;Jiang, W.;Wang, Z.;Li, W.;Xie, W.;Yang, H.;Yang, W. Hewettite $ZnV_6O_{16}\cdot 8H_2O$ with Remarkably Stable Layers and Ultralarge Interlayer Spacing for High-Performance Aqueous Zn-Ion Batteries. *Angew. Chem. Int. Ed.* **2023**, *62*, e202213368.

[28] Hossain, M. A.;Ahmed, F.;Srivastava, J. P. A raman spectroscopic study of tetramethylammonium tribromocadmate. *physica status solidi (a)* **1995**, *151*, 299-304.

[29] Xie, Q.;Cheng, G.;Xue, T.;Huang, L.;Chen, S.;Sun, Y.;Sun, M.;Wang, H.;Yu, L. Alkali ions pre-intercalation of δ-$MnO_2$ nanosheets for high-capacity and stable Zn-ion battery. *Mater. Today Energy* **2022**, *24*, 100934.

[30] Chomkhuntod, P.;Hantanasirisakul, K.;Duangdangchote, S.;Phattharasupakun, N.;Sawangphruk, M. The charge density of intercalants inside layered birnessite manganese oxide nanosheets determining Zn-ion storage capability towards rechargeable Zn-ion batteries. *J. Mater. Chem. A* **2022**, *10*, 5561-5568.

[31] Li, Y.;Li, X.;Duan, H.;Xie, S.;Dai, R.;Rong, J.;Kang, F.;Dong, L. Aerogel-structured $MnO_2$ cathode assembled by defect-rich ultrathin nanosheets for zinc-ion batteries. *Chem. Eng. J.* **2022**, *441*, 136008.

[32] Zheng, Z.;Yang, G.;Yao, J.;Li, J.;Zheng, J.;Wu, Z.;Gan, Y.;Wang, C.;Lv, L.;Wan, H.;Chen, C.;Wang, H.;Tao, L.;Zhang, J.;Wang, H. High-valence molybdenum promoted proton migration and inhibited dissolution for long-life aqueous Zn-$MnO_2$ batteries. *Appl. Surf. Sci.* **2022**, *592*, 153335.

[33] Lv, W.;Meng, J.;Li, Y.;Yang, W.;Tian, Y.;Lyu, X.;Duan, C.;Ma, X.;Wu, Y. Inexpensive and eco-friendly nanostructured birnessite-type δ-$MnO_2$: A design strategy from oxygen defect engineering and $K^+$ pre-intercalation. *Nano Energy* **2022**, *98*, 107274.

[34] Chen, H.;Ma, W.;Guo, J.;Xiong, J.;Hou, F.;Si, W.;Sang, Z.;Yang, D. a. PEDOT-intercalated $MnO_2$ layers as a high-performance cathode material for aqueous Zn-ion batteries. *J. Alloys Compd.* **2023**, *932*, 167688.

[35] Zuo, Y.;Meng, T.;Tian, H.;Ling, L.;Zhang, H.;Zhang, H.;Sun, X.;Cai, S. Enhanced $H^+$ Storage of a $MnO_2$ Cathode via a $MnO_2$ Nanolayer Interphase Transformed from Manganese Phosphate. *ACS Nano* **2023**, *17*, 5600-5608.

[36] Wang, D.;Liu, Z.;Gao, X.-W.;Gu, Q.;Zhao, L.;Luo, W.-B. Massive anionic fluorine substitution two-dimensional δ-$MnO_2$ nanosheets for high-performance aqueous zinc-ion battery. *J. Energy Storage* **2023**, *72*, 108740.

[37] Naresh, N.;Eom, S.;Lee, S. J.;Jeong, S. H.;Jung, J. W.;Jung, Y. H.;Kim, J. H. Disordered Structure and Reversible Phase Transformation from K-Birnessite to Zn-Buserite Enable High-Performance Aqueous Zinc-Ion Batteries. *Energy Environ. Mater.* **2023**, 12640.

[38] Lam, D. V.;Dung, D. T.;Kim, J.-H.;Lee, S.-M. Metal–Organic Framework-Derived NiO@C as a Host for $MnO_2$ Cathode of Stable Zinc-Ion Batteries. *ACS Appl. Energy Mater.* **2023**, *6*, 5368-5377.

[39] Liu, L.;Wu, Y. C.;Huang, L.;Liu, K.;Duployer, B.;Rozier, P.;Taberna, P. L.;Simon, P. Alkali Ions Pre-Intercalated Layered $MnO_2$ Nanosheet for Zinc-Ions Storage. *Adv. Energy Mater.* **2021**, *11*, 3101287.

[40] Sun, T. J.;Nian, Q. S.;Zheng, S. B.;Shi, J. Q.;Tao, Z. L. Layered Ca0.28MnO2•0.5H2O as a High Performance Cathode for Aqueous Zinc-Ion Battery *Small* **2020**, *16*, 2000597.

[41] Fang, G.;Zhu, C.;Chen, M.;Zhou, J.;Tang, B.;Cao, X.;Zheng, X.;Pan, A.;Liang, S. Suppressing Manganese Dissolution in Potassium Manganate with Rich Oxygen Defects Engaged High-Energy-Density and Durable Aqueous Zinc-Ion Battery. *Adv. Funct. Mater.* **2019**, *29*, 1808375.

[42] Huang, T.;Cheng, M.;Yuan, Y.;Kong, L.;Chang, Z.;Bu, X.-H. Fabrication of N-doped carbon-coated MnO/$ZnMn_2O_4$ cathode materials for high-capacity aqueous zinc-ion batteries. *Dalton Trans.* **2023**, *52*, 13737-13744.

[43] Nam, K.-W.;Kim, M. G.;Kim, K.-B. In Situ Mn K-edge X-ray Absorption Spectroscopy Studies of Electrodeposited Manganese Oxide Films for Electrochemical Capacitors. *J. Phys. Chem. C* **2007**, *111*, 749-758.

[44] Gao, P.;Metz, P.;Hey, T.;Gong, Y.;Liu, D.;Edwards, D. D.;Howe, J. Y.;Huang, R.;Misture, S. T. The critical role of point defects in improving the specific capacitance of delta-$MnO_2$ nanosheets. *Nat. Commun.* **2017**, *8*, 14559.

[45] Chao, D.;Ye, C.;Xie, F.;Zhou, W.;Zhang, Q.;Gu, Q.;Davey, K.;Gu, L.;Qiao, S. Z. Atomic Engineering Catalyzed $MnO_2$ Electrolysis Kinetics for a Hybrid Aqueous Battery with High Power and Energy Density. *Adv. Mater.* **2020**, *32*, e2001894.

[46] Poyraz, A. S.;Huang, J.;Pelliccione, C. J.;Tong, X.;Cheng, S.;Wu, L.;Zhu, Y.;Marschilok, A. C.;Takeuchi, K. J.;Takeuchi, E. S. Synthesis of cryptomelane type α-$MnO_2$($KxMn_8O_{16}$) cathode materials with tunable $K^+$ content: the role of tunnel cation concentration on electrochemistry. *J. Mater. Chem. A*, **2017**, *5*, 16914-16928.

[47] Zhang, R.;Yu, X.;Nam, K.-W.;Ling, C.;Arthur, T. S.;Song, W.;Knapp, A. M.;Ehrlich, S. N.;Yang, X.-Q.;Matsui, M. α-$MnO_2$ as a cathode material for rechargeable Mg batteries. *Electrochem. Commun.* **2012**, *23*, 110-113.

[48] Han, S.-D.;Kim, S.;Li, D.;Petkov, V.;Yoo, H. D.;Phillips, P. J.;Wang, H.;Kim, J. J.;More, K. L.;Key, B.;Klie, R. F.;Cabana, J.;Stamenkovic, V. R.;Fister, T. T.;Markovic, N. M.;Burrell, A. K.;Tepavcevic, S.;Vaughey, J. T. Mechanism of Zn Insertion into Nanostructured δ-$MnO_2$: A Nonaqueous Rechargeable Zn Metal Battery. *Chem. Mater.* **2017**, *29*, 4874-4884.

## Declaration of interests

☒The authors declare that they have no known competing financial interests or personal relationships that could have appeared to influence the work reported in this paper.

☐The authors declare the following financial interests/personal relationships which may be considered as potential competing interests: